The impact of heavy Ga doping on superconductivity in germanium

R. Skrotzki[1,2], T. Herrmannsdörfer[1], V. Heera[1], J. Fiedler[1], A. Mücklich[1], M. Helm[1], and J. Wosnitza[1]

[1]*Dresden High Magnetic Field Laboratory (HLD) and Institute of Ion Beam Physics and Materials Research, Helmholtz-Zentrum Dresden-Rossendorf (HZDR), D-01314 Dresden, Germany*
E-mail: j.wosnitza@hzdr.de

[2]*Department of Chemistry and Food Chemistry, TU Dresden, D-01062 Dresden, Germany*

We report new experimental results on how superconductivity in gallium-doped germanium (Ge:Ga) is influenced by hole concentration and microstructure. Ion implantation and subsequent flash-lamp annealing at various temperatures have been utilized to prepare highly *p*-doped thin films consisting of nanocrystalline and epitaxially grown sublayers with Ga-peak concentrations of up to 8 at.%. Successive structural investigations were carried out by means of Rutherford-backscattering spectrometry in combination with ion channelling, secondary-ion-mass spectrometry, and high-resolution cross-sectional transmission electron microscopy. Hole densities of $1.8 \cdot 10^{20}$ to $5.3 \cdot 10^{20}$ cm^{-3} (0.4 to 1.2 at.%) were estimated via Hall-effect measurements revealing that only a fraction of the incorporated gallium has been activated electrically to generate free charge carriers. The coincidence of a sufficiently high hole and Ga concentration is required for the formation of a superconducting condensate. Our data reflect a critical hole concentration of around 0.4 at.%. Higher concentrations lead to an increase of T_c from 0.24 to 0.43 K as characterized by electrical-transport measurements. A short mean-free path indicates superconductivity in the dirty limit. In addition, small critical-current densities of max. 20 kA/m^2 point to a large impact of the microstructure.

Introduction

Notably, not more than one decade has passed since the sudden scientific ascent of superconductivity in covalent-bound materials [1,2]. Highly doped diamond [3], silicon [4], and germanium [5] — classic group-IV semiconductors — surprisingly turned out to be low-temperature superconductors. However, to achieve this, doping concentrations beyond the metal-to-insulator transition (MIT) had to be incorporated.

Motivated by the first observations of ambient-pressure superconductivity in boron-doped diamond (BDD), silicon (Si:B), and gallium-doped germanium, methods of increasing the critical temperature (T_c) had soon been sought after. Thus, new state-of-the-art nonequilibrium preparation techniques were applied to realize even higher doping levels. Replacing high-pressure high-temperature synthesis by chemical vapor deposition successfully increased T_c of BDD from around 4 to more than 7 K [3,6]. Alternatively, improved gas-immersion laser doping (rising T_c from 0.4 to 0.6 K in Si:B) [4,7] and enhanced ion implantation accompanied by flash-lamp or rapid thermal annealing (rising T_c from 0.5 to 1.2 K in Ge:Ga) [5,8] have been demonstrated.

However, a thorough analysis is required in order to find out which key features really tend to trigger superconductivity in covalent-bound materials. Of course, most insight is expected studying the role of the dopant concentration, i.e., in particular the charge-carrier density. It was found that above a certain concentration, usually tagged as critical doping level, superconductivity emerges. Close to this point, T_c rises steeply and seems to saturate at higher concentrations [7,9,10].

Achieving a comprehensive picture is complicated when considering a general lack of comparability among sample series prepared differently. For instance, crystal orientation

during doping processes have been reported to play a crucial role [11]. Since nonequilibrium preparations almost inevitably introduce disorder down to the atomic scale, its impact on superconductivity — which up to now remains uncertain — must be considered. While most reports unveil critical fields in the Tesla range, thus obviously indicating type-II superconductivity, recent investigations on more homogeneously doped Si:B samples give rise to a possible intrinsic type-I character that may artificially be hidden due to mean-free path and Ginzburg–Landau coherence-length restrictions, respectively [7]. Further physical properties may change when extraordinarily high dopant concentrations of often more than 10 at.% are incorporated. That is why further insight in microstructure and local analysis is highly desirable. Most important recent work include angle-resolved photo-emission spectroscopy [12] and low-temperature scanning tunnelling microscopy (STM) [13–15]. The former indicated that diamond valence-band holes establish the Fermi surface of BDD, thus rendering a possible impurity-band scenario unlikely. STM data revealed that Si:B epilayers exhibit BCS-like superconductivity [13] while in nanocrystalline BDD the proximity effect has been found [14,15]. A distinct carbon but less clear boron isotope effect has further unraveled the phonon-mediated nature of superconductivity in BDD [16,17]. All these findings favor conventional superconductivity which is well confirmed within a theoretical approach pronouncing similarities of Cooper pairing in heavily doped diamond, silicon, and germanium to superconductivity in magnesium diboride [18].

Focussing on heavily gallium-doped germanium, the most recently discovered hence least explored of the above-mentioned superconductors, we will present new results on the evolution of T_c with charge-carrier concentration. By studying a large number of samples prepared differently, further light is shed on the impact of microstructure, i.e., Ga distribution and crystallinity. Moreover, critical-field and critical-current density measurements unravel the underlying character of superconductivity.

Preparation methods

In order to incorporate high charge-carrier densities in semiconductors, dopants with large solid solubilities are favorable. Unlike for diamond and silicon, boron doping, so far, has failed to establish superconductivity in germanium [19]. Gallium — adjacent to germanium in the periodic table of elements — is a better choice. Because of its similar covalent radius it allows for the highest charge-carrier activation in germanium among all possible elements [20]. Thus, the solubility limit of gallium in germanium ($4.9 \cdot 10^{20}$ cm^{-3}) is almost two orders of magnitude larger than reported for boron ($5.5 \cdot 10^{18}$ cm^{-3}) [21]. Due to high-mobility Ge valence-band holes, the metal-to-insulator transition in Ge:Ga occurs already at $1.9 \cdot 10^{17}$ cm^{-3} [22].

In contrast, concentrations of more than 10^{20} cm^{-3} are required for the MIT in BDD [3].

Ion implantation, known as the standard process for selected-area doping in silicon-based microelectronic technology [23], may be also a key process in the fabrication of future germanium-based electronic devices [24]. It allows for a very reproducible and well controllable realization of dopant profiles ranging from several μm down to some nm in depth. For that reason, it provides a versatile tool that can be utilized for nonequilibrium high-dose doping processes as required for Ge:Ga. However, high-dose ion implantation causes severe lattice damages as well. The latter, noticeable as substrate amorphization in Ge:Ga, has to be annealed subsequently to the implantation process. Therefore, a short-time thermal treatment at temperatures close to but still below the melting point is applied. Furthermore, this step is necessary to activate the implanted atoms electrically, i.e., to adapt them to substitutional lattice positions. Though, one has to consider that depending on the annealing temperature, there is an exposure-time window, defined as the time when solid-phase epitaxy (SPE) or random-nucleation and growth (RNG) has taken place, but dopant diffusion, thus possible segregation, has not yet started. Approaching the melting temperature, this favorable window becomes narrow, though still being accessible via novel annealing processes like flash-lamp annealing (FLA) providing high-intensity infrared to optic light pulses in the ms range.

In our previous investigations, flash-lamp or rapid thermal annealing (RTA) were accompanied by an emerging dopant diffusion and, finally, a loss of dopant atoms through out-diffusion at higher temperatures [5,8]. As a consequence, superconductivity has been excluded or at least shifted to lower temperatures in the samples where a loss of dopants has been observed. This has motivated the present work where the annealing — restricted to FLA here — is varied in small steps throughout a series of seven samples. Causing slight, hence less dramatic changes in the electronic and structural properties, we have been able to study the impact on superconductivity in more detail.

Measurement technique

We have used commercial <100>-oriented 2″ Ge wafers as substrates. The wafers had initially been slightly *n* doped by antimony (10^{14} cm^{-3}) to keep leakage currents low due to the formation of a space-charge zone upon *p* doping. To prevent surface degradation during implantation, an additional 30 nm SiO$_2$ capping has been sputtered on top of the wafers. Implantation has been carried out with 100 keV Ga$^+$ ions at a total dose of $2 \cdot 10^{16}$ cm^{-2}, equal to our previous investigations [5,8]. Though, further samples with a lower dose, $0.6 \cdot 10^{16}$ cm^{-2}, have been prepared for comparison. After implantation, the samples were cut into 1×1 cm pieces. As second processing step, FLA in flowing Ar gas
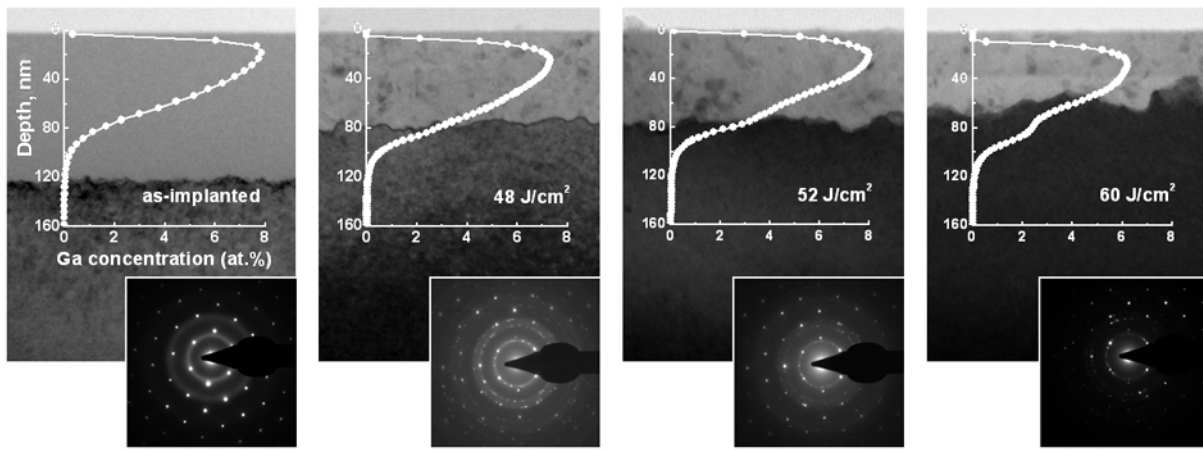
Fig. 1. High-resolution cross-sectional transmission electron micrographs revealing the microstructure of Ge:Ga. The bright-colored implantation-induced amorphous surface region becomes nanocrystalline upon flash-lamp annealing. Further, a gradual solid-phase epitaxial regrowth starting from the dark single crystalline substrate takes place. The diffraction patterns of the displayed regions support these findings. In addition, Ga-depth profiles have been measured via secondary ion mass spectrometry.

at 3 ms constant light-pulse duration and total energy densities, i.e., fluences of 46–60 J/cm^2 has been applied. During the pulses, the surface of the samples heats up to temperatures ranging from 700°C (lowest fluence) to slightly below the melting temperature of Ge (highest fluence). An estimate of the thermal evolution and distribution during FLA — sensitively depending on the optical and thermal properties of the sample — is given in Ref. 20. Finally, the samples were etched in fluoric acid to remove the SiO$_2$ cover which is necessary for electrical transport measurements.

The structure of Ge:Ga has been analyzed by means of Rutherford-backscattering spectrometry with 1.7 MeV He$^+$ ions in combination with ion channelling (RBS/C). Further, the Ga-depth distribution has been measured via secondary ion mass spectrometry (SIMS) using an O^{2+} ion beam. In addition, high-resolution cross-sectional transmission electron microscopy (XTEM) has been carried out to study the morphology of Ge:Ga using an image-corrected FEI Titan 80-300 transmission electron microscope. Selected-area diffraction patterns were taken to search for Ga-related precipitates.

Hall-effect measurements have been performed at temperatures between 2 and 400 K by using a commercial system (Lakeshore Model 9709A). The charge-carrier density and mobility were determined via the "Van-der-Pauw" method, while low-temperature transport measurements were carried out in the usual four-terminal geometry. For the latter, a self-built insert making use of adiabatic demagnetization of a paramagnetic salt installed in a commercial magnet-cryostat system allowed for reaching minimum temperatures of around 80 mK. Ohmic contacts have either been realized by use of silver glue and indium or via sufficient mechanical pressure.

Crystal structure and the normal state

Ion implantation at $2 \cdot 10^{16}$ cm^{-2} results in a Gaussian Ga-depth profile with a maximum concentration of 8 at.% ($3.6 \cdot 10^{21}$ cm^{-3}) and a FWHM of roughly 60 nm situated at a depth of around 20 nm as revealed by SIMS measurements (Fig. 1). These findings match well with the prediction of simulations [25]. Due to the implantation damage, a 120 nm thick layer beneath the surface becomes amorphous. This feature is reflected by a clear TEM contrast (Fig. 1) and a near-surface RBS/C peak reaching the intensity of the spectrum that has been measured in random orientation (Fig. 2). While in this case RBS/C is not sensi-
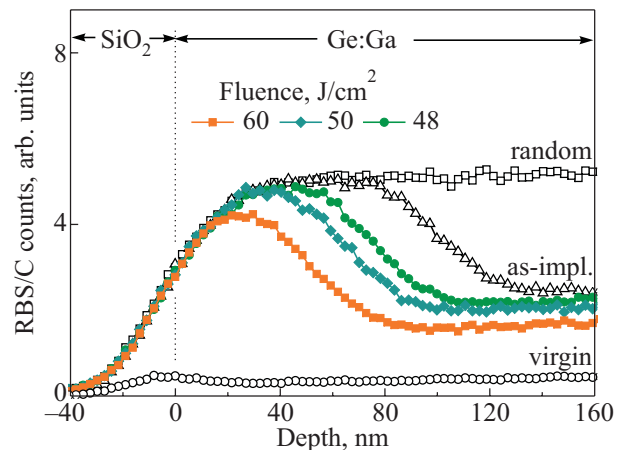

Fig. 2. (Color online) Depth-calibrated spectra of Rutherford backscattering on Ge and Ga atoms using ion channelling (measured prior to the SiO$_2$ etching). The backscattering rate is proportional to the amount of local lattice misorientation in respect to the single crystalline substrate (virgin). Near-surface peaks reach the maximum scattering rate as referenced by the random orientation spectrum, though having different origins (Fig. 1) as annealing forms a nanocrystalline layer out of the previously amorphous region (as-implanted). A gradual epitaxial regrowth starting from the substrate occurs with increasing FLA fluence.

tive to distinguish between polycrystalline and amorphous areas, broad rings in the selected-area diffraction pattern give rise to an amorphous structure. However, deeper-lying (depth > 120 nm) Ge layers remain single crystalline indicated by characteristic Ge diffraction patterns. Flash-lamp annealing changes the morphology. On the one hand, the previously amorphous near-surface region transforms into a polycrystalline layer with grain sizes of 5 to 15 nm resulting in thin TEM diffraction rings (Fig. 1). These grains grow with increasing fluence and are visible as dark XTEM spots (Fig. 1). On the other hand, we observe a gradual solid-phase epitaxial regrowth from the substrate towards the surface which reduces the polycrystalline area to a minimum thickness of approximately 60 nm at 60 J/cm^2. The high amount of Ga and intermixed atoms from the SiO$_2$ capping most probably act as nucleation spots for a catalyzed crystallization which prevents a full epitaxial regrowth. The latter has been observed for an implantation dose of $0.6 \cdot 10^{16}$ cm^{-2} [20]. Remarkably, the Ga distribution did not change significantly during FLA (Fig. 1). Although a closer look reveals an evolving kink in the profiles located at the boundary between poly- and single crystalline regions. This may be explained by different diffusion rates. Additionally, a Ga loss through the surface is observed affecting the maximum concentration that is reduced to 6.2 at.% at 60 J/cm^2. To exclude possible foreign phases, an extensive XTEM search via sample tilting and spatial Fourier transformation has been carried out. Since the binary phase diagram of Ge:Ga features only an eutectic mixture of almost pure Ga (with 0.006 at.% Ge), solely clusters of the latter and no further intermetallic phases would be expected [26]. After all, in none of our samples clusters have been found. However, segregations of less than 3 nm cannot be excluded within our microscopic resolution.

As one may expect, also the electronic properties are clearly affected by each preparation step. Temperature-dependent resistivity measurements of the virgin Ge substrate, as-implanted Ge:Ga, and FLA Ge:Ga are presented in Fig. 3. Upon cooling, the virgin substrate's resistivity first decreases due to a rising charge-carrier mobility, but finally exhibits a typical semiconducting behavior. The as-implanted sample shows a more complicated dependence as leakage currents through the substrate have to be taken into account at higher temperatures. Towards low temperatures, the resistivity increases indicating a potential hopping conductivity. This is a striking evidence for insufficient dopant activation in the amorphous surface region. Upon annealing, Ge:Ga finally shows metallic conductivity and, furthermore, a reasonable low-temperature resistivity of about 10^{-3}–10^{-4} Ω·cm before the superconducting transition at around 0.5 K sets in. The double-logarithmic scale in Fig. 3 emphasizes how dramatic the transport behavior can be influenced by controlled preparation methods. As will be outlined below, the transport and especially the
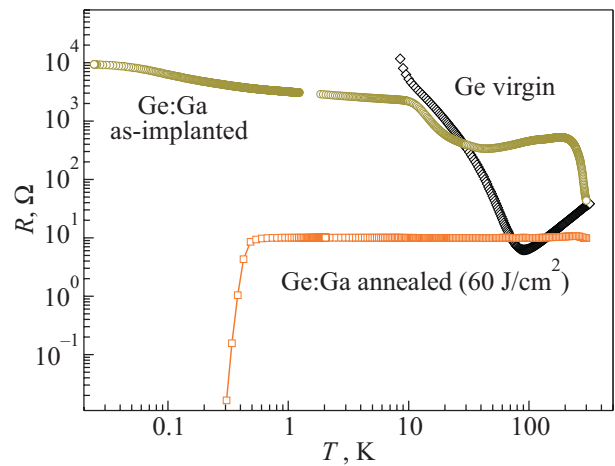

Fig. 3. (Color online) Temperature dependence of the resistance for different preparation steps. While the virgin substrate reveals a typical semiconducting behavior and as-implanted Ge:Ga is highly resistive at low temperatures, annealed Ge:Ga shows metallic conductivity and superconductivity below approximately 0.5 K.

superconducting properties of annealed Ge:Ga depend sensitively on the applied FLA fluences. At temperatures of around 260 to 270 K, the annealed Ge:Ga samples reveal a crossover from electron- to hole-like conductivity. This indicates that leakage currents through the *n*-doped substrate are dominating the electronic transport at higher temperatures. Thus, Hall-effect measurements for estimating the charge-carrier density and mobility have been performed at 3 K. Since the magnetoresistance does not exceed 10% at fields of 9 T, a one-band interpretation of the Hall-effect proves to be reasonable within the uncertainties that are implicated by electrical transport through a multi-layered system. As already shown in Fig. 3, annealed Ge:Ga exhibits a substantial small residual resistivity ratio (RRR) of the order 1 indicating that Ge:Ga is a "bad" metal. Low hole mobilities of around 40 cm^2/(V·s) in all annealed samples reflect the short mean-free paths originating from the disordered and mainly nanocrystalline structure. Increasing the annealing fluence from 48 to 60 J/cm^2 results in a gradual drop of the low-temperature resistivity by a factor of 4 (Fig. 4). This may rather be caused via an increasing charge-carrier density (Fig. 5) than reflecting the slight improvement of sample crystallinity. Obviously, the hole activation turns out to be crucially affected upon FLA. As our Hall-effect measurements show, the latter increases nearly monotonously within our sample series, resulting in hole concentrations per area ranging from 1.9 to $4.8 \cdot 10^{15}$ cm^{-2}. The spatial activation, i.e., the hole-depth distribution remains unknown. As the thickness of the epitaxially grown layer, where — from a qualitative point of view — higher activation ratios may be expected, and the Ga profile change only slightly upon FLA, we can translate the rising sheet-carrier concentration into an increase of the spatial hole concentration. Further,
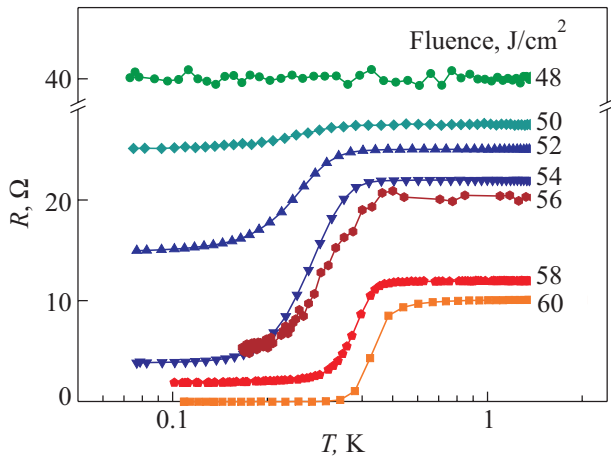
Fig. 4. (Color online) Low-temperature resistivity of Ge:Ga that has been annealed at different FLA fluences measured with an applied current of 1 μA. Rising the annealing temperature results in a higher T_c and an increased relative resistivity drop upon entering the superconducting state. Zero resistivity at $T < T_c$ has only been observed after FLA at 60 J/cm^2.

we do not know whether one layer favors the occurrence of superconductivity more than the other. That is why we point out two estimates disregarding the local crystallinity. On the one hand, a spatial activation proportional to the Ga-depth profile may be conceivable. On the other hand, the formation of a hole-concentration plateau over an effective length within the implanted region renders another possible scenario. Since the latter takes into account that regions containing less Ga are activated much better in respect to their Ga concentration, it seems to be a reasonable approach. Following the latter, we derive an effective plateau length of 80–100 nm with hole densities $n_{vol} = (1.8–5.3) \cdot 10^{20}$ cm^{-3} (0.4 to 1.2 at.%). Considering Ga
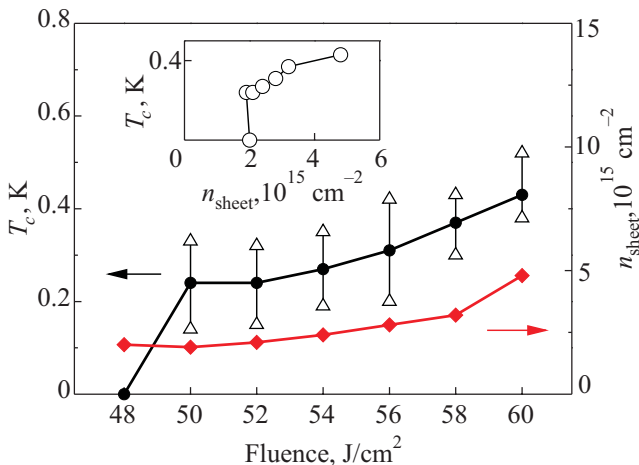

Fig. 5. (Color online) Critical temperature (left axis) and sheet-carrier concentration (right axis) of Ge:Ga plotted vs. the annealing fluence. The filled circles and open triangles mark the temperatures at 50, 10, and 90% superconducting resistivity drop (as derived from Fig. 4). A direct correlation between the concentration and T_c is assumed and plotted in the inset.

peak concentrations between 6 and 8 at.% (Fig. 1) this results in minimal local activation ratios of 5–20%. In Ref. 20, this important issue is addressed in more detail.

Superconducting properties

The low-temperature resistivity of Ge:Ga is presented in Fig. 4. The measurements were performed in zero magnetic field with excitation currents of 1 μA. The results were reproduced with currents of 100 nA indicating that no influence of the critical current density has to be considered at these measurement currents.

After annealing with a fluence of 48 J/cm^2, no superconductivity is found. As the annealing temperature is increased, superconductivity emerges at 0.24 K and gradually rises to higher temperatures. A maximum T_c of 0.43 K is reached at 60 J/cm^2 (taking the resistive midpoint as criterion). Further, the relative height of the resistivity drop also increases monotonously. In more detail, a large remnant resistivity in the superconducting state remains after FLA at 50 J/cm^2, whereas zero resistivity has been observed after FLA at 60 J/cm^2. While we attribute the rising T_c to an increase of the hole concentration, the remaining residual resistivity may be explained in terms of laterally inhomogeneous activation ratios which could result in less doped, thus nonsuperconducting regions. The evolution of the critical temperature (10, 50, and 90% of the resistance drop) and corresponding sheet-carrier concentration n_{sheet} with applied FLA fluence is shown in Fig. 5. Since crystallinity and Ga profile differ only slightly among the samples, we suggest a direct correlation between T_c and hole concentration. This would mean that the dependence outlined in the introduction seems to be valid not only for BDD and Si:B but also for Ge:Ga since we observe the following. The critical temperature of Ge:Ga rises steeply at a critical sheet concentration of about $2 \cdot 10^{15}$ cm^{-2} or a corresponding spatial density of 0.4 at.% (inset Fig. 5). For this concentration no sign of superconductivity is found down to 80 mK after FLA at 48 J/cm^2, whereas for 50 J/cm^2 superconducting traces emerge at 0.24 K. T_c increases further with hole concentration though less steeply. The transition width fluctuates nonsystematically between 0.1 and 0.2 K. As mentioned above, we further investigated a series of equally flash-lamp annealed Ge:Ga samples having an implantation dose of $0.6 \cdot 10^{16}$ cm^{-2}. We have found similar or even higher hole concentrations but no superconductivity. This means that nonactivated gallium that may be situated at interstitial lattice places, seems to be another necessary parameter (besides the charge-carrier concentration) for the occurrence of superconductivity. Whether this originates from corresponding lattice distortions, i.e., chemically induced pressure or modifications of the phonon spectra remains an open question.

After the discussion of the influence of the preparation parameters, we now focus on the properties of the super-
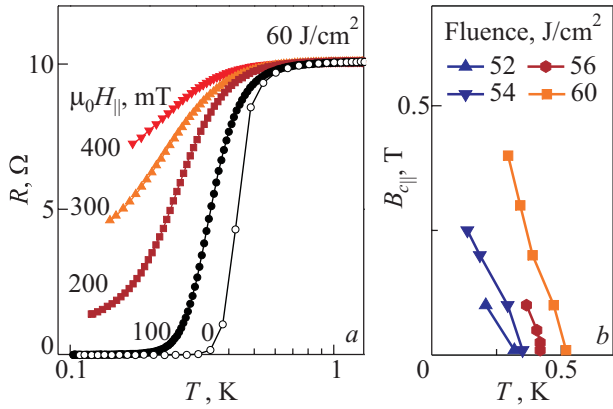
Fig. 6. (Color online) (*a*) Temperature dependence of the resistance at various in-plane magnetic fields (measured with a current of 1 μA) for the sample annealed at 60 J/cm^2. (*b*) In-plane field-temperature phase diagram of four differently annealed Ge:Ga samples. $B_{c2\parallel}(T)$ has been derived from the temperatures at which the resistivity drops by 10% at constant magnetic fields.

conducting state. We have performed electrical-transport measurements at various applied magnetic fields and with different excitation currents. In Fig. 6,*a*, the temperature-dependent resistivity of the sample with the highest T_c (60 J/cm^2) is shown for in-plane fields up to 400 mT. The broadening of the transition may be attributed to a so-called vortex-liquid state which is well known for type-II superconductors [27]. The resulting field-temperature phase-diagram of this and three other samples is drawn in Fig. 6,*b*. Here, the 10% resistivity drop of various $R(T)$ curves at constant in-plane magnetic fields has been taken as criteria for $B_{c2\parallel}(T)$. If we extrapolate the linear dependence for $T \to 0$, we find $B_{c2\parallel} \approx 0.8$ T for the sample annealed at 60 J/cm^2. A linear dependence of $B_{c2\parallel}$ down to 0.1 T_c has been revealed within our previous investigations of Ge:Ga [5]. The theory of Werthamer, Helfand, and Hohenberg describes $B_{c2}(T)$ for superconductors in the dirty limit, i.e., where the Ginzburg–Landau coherence length is restricted by short electronic mean-free paths [28–30]. This condition is fulfilled for heavily Ga-doped Ge. An estimate of the electronic mean-free path is given via $l^* = \mu v_F m_{eff}/e \approx 7$ nm, with $v_F = (\hbar/m_{eff})(3\pi^2 n_{vol})^{1/3}$ as the Fermi velocity for the maximum spatial hole density $n_{vol} = 5.3 \cdot 10^{20}$ cm^{-3}, $\mu = 40$ cm^2/(V·s) the charge carrier mobility, and m_{eff} the effective hole mass [31]. This estimate appears reasonable as the mean-free path matches well with the grain size of the nanocrystalline Ge:Ga layer. Although we have found a small anisotropy [5], the critical fields parallel and perpendicular to the layer are roughly of the order of $B_{c2} \approx 0.5$ T. This leads to a Ginzburg–Landau coherence length of $\xi_{GL} = [\phi_0/(2\pi B_{c2})]^{0.5} \approx 26$ nm, where $\phi_0 = h/2e = 2.068 \cdot 10^{-15}$ Wb is the flux quantum. Thus, ξ_{GL} is restricted by the mean-free path according to $\xi_{GL}(l^*) = = (\xi_{GL}(l^* = \infty)l^*)^{0.5}$ as $l^* < \xi_{GL}(l^* = \infty)$ [32]. With this

formula, we are able to estimate the coherence length in the clean limit $\xi_{GL}(l^* = \infty) \approx 100$ nm. Unfortunately, there was no sign of field screening detectable via ac-susceptibility measurements as possible supercurrents are strongly limited (see below). The expected Meissner signals are also below the resolution limit of our dc-susceptibility measurements. Most likely, this is related to a strong reduction of field expulsion which is common for structures smaller than or of the order of the London penetration depth λ_L [33]. Thus, λ_L and the Ginzburg–Landau parameter $\kappa_{GL} = \lambda_L/\xi_{GL}$ remain unknown. However, as the mean-free path modifies the latter via $\kappa_{GL}(l^*) \approx \kappa_{GL}(l^* = \infty) \times \times \xi_{GL}(l^* = \infty)/l^*$ [32], we see that $\kappa_{GL}(l^*)/\kappa_{GL}(l^* = \infty) > 14$ which indicates a significant structure-induced shift of superconductivity towards type-II character. Together with the high critical fields, this confirms type-II superconductivity in our samples, while in cleaner Ge:Ga this character may be less distinct.

Finally, we discuss the impact of the current density on superconductivity in Ge:Ga. Notably, even small excitation currents of 20 μA are sufficient to depress superconductivity almost completely in the sample annealed at 50 J/cm^2 (Fig. 7). The occurrence of possible heating effects can be excluded as thermometry has been checked thoroughly. Moreover, we observe a pronounced transition broadening in all samples as the current is increased from 1 to 5 μA. A possible qualitative understanding may be given in terms of an inhomogeneous lateral doping which could lead to weak links along the current paths. Thus, Josephson junctions through poorly conducting or through still nonsuperconducting but low resistive Ge grains could modify the transport behavior. However, we do not find explicit evidence for Josephson coupling as has been revealed, e.g., for superconductivity in granular cuprates [34]. There, an increase of resistivity towards lower temperatures at over-
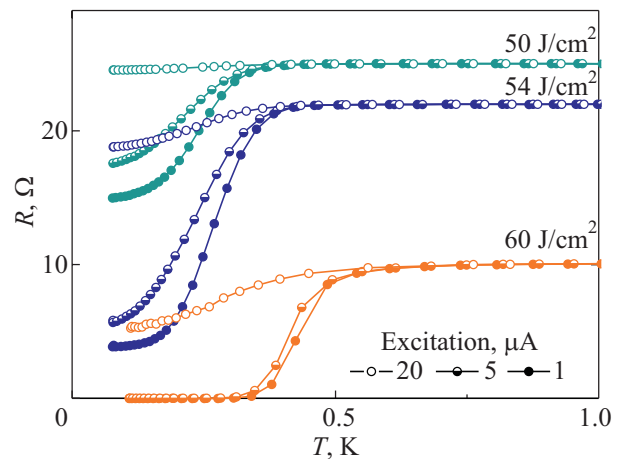

Fig. 7. (Color online) Temperature dependence of the resistance for differently annealed samples and different excitation currents. For the sample annealed at 50 J/cm^2 a current of around 20 μA (equivalent to a current density of about 20 kA/m^2) is sufficient to suppress the superconducting transition.

critical currents indicates thermal blocking of quasiparticle tunnelling. This behavior has not been observed in Ge:Ga. Further, we find that higher annealing fluences result in slightly larger critical currents. A comparison with other Ge:Ga samples unveiled that this is not a consequence of the rising T_c, but may rather be explained by the increasing crystallinity (i.e., larger grain sizes and further epitaxial regrowth) and a possibly more homogeneous dopant activation. Generally, we find very low critical-current densities down to $J_c \approx 20$ μA/(100 nm·1 cm) = 20 kA/m^2 that further need to be probed locally for better quantitative understanding.

Discussion

Triggered by our findings, *ab initio* supercell calculations based on the density-functional theory have been published recently [35]. Starting with the assumption of perfectly doped, i.e., activated Ge:Ga with a Ga concentration of 6.25 at.%, the crystal lattice has been found to be only slightly altered compared to undoped Ge while the band structure becomes significantly modified and exhibits a shift of the Fermi level to 0.6 eV below the valence-band maximum. This results in the formation of a Fermi surface emerging around the Brillouin-zone center. Consequently, the optical-phonon spectrum becomes softened and new gallium-associated modes arise. These findings are well confirmed by a second approach that further includes an investigation of the electron–phonon coupling and its impact on T_c [36]. The latter has been evaluated using the Allen–Dynes modification [37] of McMillan's solution of the Eliashberg equation [38]. In accordance to BDD and Si:B, the main contribution to the electron–phonon coupling ($\lambda = 0.35$) is assigned to optical-phonon modes (75%). While these are attributed to the Ge lattice, the acoustic modes are associated with the incorporated gallium content. Most interestingly, the latter account for 25% of the coupling featuring a significant impact of the dopant atom on the BCS-like superconductivity identified for Ge:Ga.

We now want to discuss our experimental results in the context of superconductivity in heavily doped group-IV semiconductors. We find that the qualitative doping dependence of Ge:Ga is in good agreement with previous observations in BDD and Si:B [7,9]. Also the critical hole concentrations of 0.5 at.% ($0.9 \cdot 10^{21}$ cm^{-3}) [9] in BDD and 2 at.% ($1 \cdot 10^{21}$ cm^{-3}) [7] in Si:B are comparable to our finding of 0.4 at.% ($0.2 \cdot 10^{21}$ cm^{-3}) in Ge:Ga. However, a quantitative description in terms of an universal understanding requires further knowledge about the role of the dopants. Theoretical investigations which focus roughly on treating the latter as source of charge carriers lead to an underestimation of critical temperatures as the predicted crucial doping levels lie above those which have been found experimentally [18]. Within this work, we have shown that especially for Ge:Ga the activation ratio of dopants may play an important though previously unconsi-

dered role. A critical charge-carrier concentration of about 0.4 at.% has been found in the vicinity of a maximum Ga concentration of 8 at.%. This reflects the presence of mainly electrically nonactivated gallium. Furthermore, in case of an implantation dose about three times smaller, similar and even higher hole concentrations did not result in superconductivity. This obviously calls for a more sophisticated influence of the incorporated gallium.

As we are facing a large amount of nonactivated gallium and are dealing with concentrations above the solubility limit, the issue of possible Ga segregation has to be discussed seriously, although no traces of Ga clusters have shown up in our XTEM investigations. Several superconducting Ga phases are known. The standard α phase has a T_c of 1.08 K. Further crystalline phases reveal critical temperatures between 6.07 and 7.85 K [39]. Amorphous Ga reveals a more complex behavior as superconductivity in disordered thin films depends sensitively not only on film thickness but also on chemical surrounding, i.e., the substrate used for film growth [40,41]. Furthermore, the normal-state low-temperature thin-film sheet resistance seems to play a crucial role, as $R_q \approx 6.45$ kΩ/sq. manifests as material-independent universal upper threshold for the occurrence of superconductivity [42]. Approaching R_q, quantitative differences have been found as T_c can decrease considerably. However, all these critical temperatures are well above those which we have found in Ge:Ga. One should further mention that amorphous Ga with a diameter smaller than 1.3 nm — which could not have been detected via XTEM — was classified as nonsuperconducting [40]. Most conclusively, recent studies on Ga-implanted silicon have shown that amorphous Ga-rich precipitates can form upon subsequent rapid thermal annealing [43]. Exceeding R_q or not, they remain resistive or reveal superconductivity with an invariable T_c of 7 K. We deduce that Ga clusters prepared under such comparable though less favorable doping conditions (lower solubility of Ga in Si, higher implantation dose, longer annealing time) do not feature low-temperature superconductivity setting in at around 0.5 K which thus can be considered as intrinsic property of Ge:Ga.

Conclusion

In summary, we have unraveled the evolution of T_c with hole concentration in heavily Ga-doped germanium. In addition to a high hole concentration (> 0.4 at.%) provided by Ga acceptors the presence of a sufficiently high total Ga concentration in the range of several at.% is essential for the occurrence of superconductivity in Ge. The disordered and mainly nanocrystalline structure of Ge:Ga, as revealed by RBS/C, SIMS, and XTEM, has a decisive impact on superconductivity as the critical currents are strongly reduced. Moreover, this structure enhances the type-II character with comparably large critical fields. So far, electrical-transport measurements have been the only

way to characterize the superconducting state in thin-film Ge:Ga.

Although this work sheds light on the underlying fundamental physics, the application potential of covalent-bound superconductors is worth mentioning. Due to the preparation being fully compatible with state-of-the-art semiconductor processing thin-film Ge:Ga could easily be patterned into custom-designed devices where combined semi- and superconducting circuits may be integrated close-by [8]. Besides the small critical temperatures, first achievements concerning BDD have been reported and may stimulate further progress [44].

1. X. Blasé, E. Bustarret, C. Chapelier, T. Klein, and C. Marcenat, *Nature Mater.* **8**, 375 (2009).

2. K. Iakoubovskii, *Cent. Eur. J. Phys.* **7**, 654 (2009).

3. E.A. Ekimov, V.A. Sidorov, E.D. Bauer, N.N. Mel'nik, N.J. Curro, J.D. Thompson, and S.M. Stishov, *Nature (London)* **428**, 542 (2004).

4. E. Bustarret, C. Marcenat, P. Achatz, J. Kacmarcik, F. Lévy, A. Huxley, L. Ortéga, E. Bourgeois, X. Blasé, D. Débarre, and J. Boulmer, *Nature (London)* **444**, 465 (2006).

5. T. Herrmannsdörfer, V. Heera, O. Ignatchik, M. Uhlarz, A. Mücklich, M. Posselt, H. Reuther, B. Schmidt, K.-H. Heinig, W. Skorupa, M. Voelskow, C. Wündisch, R. Skrotzki, M. Helm, and J. Wosnitza, *Phys. Rev. Lett.* **102**, 217003 (2009).

6. Y. Takano, M. Nagao, I. Sakaguchi, M. Tachiki, T. Hatano, K. Kobayashi, H. Umezawa, and H. Kawarada, *Appl. Phys. Lett.* **85**, 2851 (2004).

7. C. Marcenat, J. Kacmarcik, R. Piquerel, P. Achatz, G. Prudon, C. Dubois, B. Gautier, J.C. Dupuy, E. Bustarret, L. Ortega, T. Klein, J. Boulmer, T. Kociniewski, and D. Débarre, *Phys. Rev.* **B81**, 020501(R) (2010).

8. T. Herrmannsdörfer, R. Skrotzki, V. Heera, O. Ignatchik, M. Uhlarz, A. Mücklich, M. Posselt, B. Schmidt, K.-H. Heinig, W. Skorupa, M. Voelskow, C. Wündisch, M. Helm, and J. Wosnitza, *Supercond. Sci. Technol.* **23**, 034007 (2010).

9. E. Bustarret, J. Kacmarcik, C. Marcenat, E. Gheeraert, C. Cytermann, J. Marcus, and T. Klein, *Phys. Rev. Lett.* **93**, 237005 (2004).

10. B. Sopík, *New J. Phys.* **11**, 103026 (2009).

11. Y. Kato, F. Matsui, T. Shimizu, H. Daimon, T. Matsushita, F.Z. Guo, and T. Tsuno, *Appl. Phys. Lett.* **91**, 251914 (2007).

12. T. Yokoya, T. Nakamura, T. Matsushita, T. Muro, Y. Takano, M. Nagao, T. Takenouchi, H. Kawarada, and T. Oguchi, *Nature* **438**, 647 (2005).

13. F. Dahlem, T. Kociniewski, C. Marcenat, A. Grockowiak, L.M.A. Pascal, P. Achatz, J. Boulmer, D. Débarre, T. Klein, E. Bustarret, and H. Courtois, *Phys. Rev.* **B82**, 140505(R) (2010).

14. F. Dahlem, P. Achatz, O.A. Williams, D. Araujo, E. Bustarret, and H. Courtois, *Phys. Rev.* **B82**, 033306 (2010).

15. F. Dahlem, P. Achatz, O.A. Williams, D. Araujo, H. Courtois, and E. Bustarret, *Phys. Status Solidi* **A207**, 2064 (2010).

16. N. Dubrovinskaia, L. Dubrovinsky, T. Papageorgiou, A. Bosak, M. Krisch, H.F. Braun, and J. Wosnitza, *Appl. Phys. Lett.* **92**, 132506 (2008).

17. V.A. Sidorov and E.A. Ekimov, *Diamond Rel. Mater.* **19**, 351 (2010).

18. L. Boeri, J. Kortus, and O.K. Andersen, *Phys. Rev. Lett.* **93**, 237002 (2004).

19. D. Cammileri, F. Fossard, D. Débarre, C. Tran Manh, C. Dubois, E. Bustarret, C. Marcenat, P. Achatz, D. Bouchier, and J. Boulmer, *Thin Solid Films* **517**, 75 (2008).

20. V. Heera, A. Mücklich, M. Posselt, M. Voelskow, C. Wündisch, B. Schmidt, R. Skrotzki, K.-H. Heinig, T. Herrmannsdörfer, and W. Skorupa, *J. Appl. Phys.* **107**, 053508 (2010).

21. F.A. Trumbore, *Bell Syst. Tech. J.* **39**, 205 (1960).

22. K.M. Itoh, E.E. Haller, J.W. Beemann, W.L. Hansen, J. Emes, L.A. Reichertz, E. Kreysa, T. Shutt, A. Cummings, W. Stockwell, B. Sadoulet, J. Muto, J.W. Farmer, and V.I. Ozhogin, *Phys. Rev. Lett.* **19**, 4058 (1996).

23. E. Rimini, *Ion Implantation: Basics to Device Fabrication*, Kluwer Academic Publisher (1995).

24. *Germanium-Based Technologies — From Materials to Devices*, C. Claeys and E. Simoen (eds.), Elsevier (2007).

25. J.F. Ziegler, J.P. Biersack, and U. Littmark, *The Stopping and Range of Ions in Solids*, Pergamon, New York (1985).

26. M. Hansen, *Constitution of Binary Alloys*, 2nd ed., McGraw-Hill Book Company Inc. (1958).

27. B.I. Halperin, G. Refael, and E. Demler, *Resistance in Superconductors* in L.N. Cooper and D. Feldman (eds.), *BCS: 50 Years*, World Scientific (2010).

28. E. Helfand and N.R. Werthamer, *Phys. Rev. Lett.* **13**, 686 (1964).

29. E. Helfand and N.R. Werthamer, *Phys. Rev.* **147**, 288 (1966).

30. N.R. Werthamer, E. Helfand, and P.C. Hohenberg, *Phys. Rev.* **147**, 295 (1966).

31. A. Dargys and J. Kundrotas, *Handbook on Physical Properties of Ge, Si, GaAs and InP*, Science and Encyclopedia Publisher, Vilnius (1994).

32. W. Buckel and R. Kleiner, *Superconductivity: Fundamentals and Applications*, Second Revised and Enlarged Edition, Wiley-VCH (2004).

33. D. Shoenberg, *Proc. R. Soc. Lond.* **A175**, 49 (1940).

34. A. Gerber, T. Grenet, M. Cyrot, and J. Beille, *Phys. Rev. Lett.* **65**, 3201 (1990).

35. S. Lebègue, *Phys. Status Solidi: Rapid Res. Lett.* **3**, 224 (2009).

36. D. Jun, L. Zhen-Yu, and Y. Jin-Long, *Chin. Phys. Lett.* **27**, 086102 (2010).

37. P.B. Allen and R.C. Dynes, *Phys. Rev.* **B12**, 905 (1975).

38. W.L. McMillan, *Phys. Rev.* **167**, 331 (1968).

39. D. Teske and J.E. Drumheller, *J. Phys.*: *Condens. Matter* **11**, 4935 (1999).

40. H.M. Jaeger, D.B. Haviland, A.M. Goldman, and B.G. Orr, *Phys. Rev. Lett.* **34**, 4920 (1986).

41. I.A. Parshin, I.L. Landau, and L. Rinderer, *Phys. Rev.* **B54**, 1308 (1996).

42. H.M. Jaeger, D.B. Haviland, B.G. Orr, and A.M. Goldman, *Phys. Rev.* **B40,** 182 (1989).

43. R. Skrotzki, J. Fiedler, T. Herrmannsdörfer, V. Heera, M. Voelskow, A. Mücklich, B. Schmidt, W. Skorupa, G. Gobsch, M. Helm, and J. Wosnitza, *Appl. Phys. Lett.* **97**, 192505 (2010).

44. S. Mandal, C. Naud, O.A. Williams, E. Bustarret, F. Omnès, P. Rodière,T. Meunier, L. Saminadayar, and C. Bäuerle, *Nanotechnology* **21**, 195303 (2010).